Numerical simulation of flight effect on the afterburning plume exhausting from a solid rocket motor

Adrien Langenais, Juliette Aubrée, Pierre Doublet, Stéphane Langlois, Valérie Rialland

DOI: ADD DOINUMBER HERE

Numerical simulation of flight effect on the afterburning plume exhausting from a solid rocket motor

Adrien Langenais[⋆†], *Juliette Aubrée*[⋆⋆], *Pierre Doublet*[⋆⋆], *Stéphane Langlois*[⋆⋆⋆], *Valérie Rialland*[⋆⋆⋆]
[⋆] *DMPE, ONERA, Université Paris Saclay, F-91123 Palaiseau - France*
[⋆⋆] *DMPE, ONERA, Université de Toulouse, F-31055 Toulouse - France*
[⋆⋆⋆] *DOTA, ONERA, Université Paris Saclay, F-91123 Palaiseau - France*
adrien.langenais@onera.fr
[†]Corresponding author

Abstract

The effect of a supersonic surrounding flow on the afterburning plume exhausting from a non-aluminized solid propellant rocket motor is numerically investigated. The motor is placed in the center of an annular channel generating a Mach 1.5 co-flow. Simulations of both cases with and without the surrounding flow are performed using an axisymmetric Reynold-averaged Navier-Stokes approach. The afterburning process between ambient air and burnt propellant gases is represented by a kinetic scheme associated with a partially stirred reactor model and a local flame extinction model. The comparison with experimental measurements shows that only the extinction model allows to capture the flame lift-off behavior.

1. Introduction

Exhaust plumes from solid propellant rocket motors are the main contributors to heat fluxes on the afterbody and to vehicle infrared signatures [1], which are major concerns for the design of space launchers, missiles or warning systems. The afterburning process occurs when the hot fuel-rich burnt propellant gases containing H_2 and CO mix with O_2 from the cold ambient air. The flame generated by the combustion reaction then contributes to increase convective and radiative heat transfers.

Accurately characterizing plume afterburning is a challenging problem because of the numerous complex physical processes affecting the flow. For example, the shock cell structure and other compressibility effects may impact the mixing layer and thermal properties of the supersonic jet, as well as external flow features, flow heterogeneity and turbulence inside the motor chamber, or flow interactions with walls and particles.

The numerical simulation can provide a reliable prediction of these phenomena in realistic flight conditions, at reasonable cost, with a plume modeling based on a compressible Reynolds-averaged Navier-Stokes solver and adequate models for turbulence, finite rate chemistry and radiative transfer [2, 3]. This approach have thus been employed in past and recent numerical studies to assess the effects of altitude, body interactions [4, 5], flight or motor operating conditions [6, 7] on the plume. However, these works sometimes suffer from a lack of validation data for the afterburning flame characterization. The turbulence-chemistry interactions in the jet mixing layer are also neglected despite the possible influence on the afterburning. Calhoon *et al.* [8, 9] show for example that it could explain the abrupt afterburning shutdown observed during the flight of many systems, with important consequences on the heat fluxes and the plume signature.

The present paper aims aims to numerically investigate the effect of a supersonic surrounding flow on an afterburning plume exhausting from a non-aluminized composite solid propellant rocket motor. The case under study is introduced in Section 2. It matches a ground experiment [10, 11] where a rocket motor was placed in the center of an annular channel generating a supersonic air co-flow in order to mimic flight effects. Instrumented firing tests were carried out with and without the surrounding flow around the motor exhaust plume, respectively labeled as dynamic and static cases [12].

Corresponding simulations are performed using the numerical procedure described in Section 3, relying on an axisymmetric Reynold-Averaged Navier-Stokes (RANS) approach. A special attention is paid to the combustion and turbulence-chemistry interactions modeling as recommended. The afterburning process is represented by a skeletal kinetic scheme [13] associated with a Partially Stirred Reactor (PaSR) combustion model [14, 15] and a local

flame extinction model [8]. The computational setup is detailed and the flow solution first validated in Section 4. The flow features are then examined and confronted to the available camera measurements in Section 5. In particular, the ability of the proposed numerical procedure to predict the afterburning flame behavior and topology is discussed.

2. Case definition

2.1 Experimental setup

A solid propellant rocket motor exhausting a hot supersonic jet and an annular channel generating a cold supersonic air co-flow are considered. The setup corresponds to the ground experiment called "LP13" developed at the ONERA's Rocket Propulsion Laboratory for investigating the motor base region in representative external flow conditions [10] and validating numerical simulation [11].

The test bench, illustrated in Figure 1, is composed by three pipes (**A**) feeding an annular plenum chamber (**B**) with pressurized cold air, which is expanded through a convergent (**C**) and a divergent annular nozzle (**D**) of exit inner diameter 100 mm. The resulting supersonic annular flow exhausts from the channel at a Mach number of 1.5. The solid rocket motor chamber (**E**) is located inside the inner annular pipe. The burnt propellant gases are guided into an extension pipe with thermal protections (**F**) before being expanded through a convergent-divergent nozzle (**G**) of exit diameter 40 mm.

The firing tests reproduced in this study has been conducted with a non-aluminized composite solid propellant, commonly used for such experiments [6, 7]. It is composed of 82 % ammonium perchlorate (AP) in mass, 11 % hydroxyl-terminated polybutadiene binder (HTPB), 4.5 % dioctyl azelate (DOZ), 1 % isophorone diisocyanate (IPDI) and 1.5 % of other additives.

2.2 Available measurements

Numerous measurements have been operated during the firing tests with sensors and cameras, including pressure measurements inside the motor and the annular channel, at the nozzle exit, at the motor base [10] as well as plume radiation measurements in ultraviolet, visible and infrared wavelengths [12]. The pressure in the motor chamber is plotted as a function of time for both static and dynamic cases in Figure 2. The evolution is similar with a pressure plateau reached 2 s after the motor ignition. For comparison purposes, all the experimental data is averaged over a shared time window extending from $t = 8$ s to $t = 9.5$ s as indicated on the figure.

The present work exploits the measurements from two particular instruments for the plume characterization, the NOXANT and Phantom cameras. The NOXANT is a cryogenic middle wavelength infrared (MWIR) camera operating on a spectral band $\lambda = 2.5\,\mu$m to $\lambda = 5\,\mu$m. The resolution is 640×168 pixels at an acquisition frame rate of $f = 100$ Hz. The device provides IR radiance fields that can be averaged and converted into contrast radiance by removing the radiance measured before the firing test from the images, as given in Figure 3 for example. The

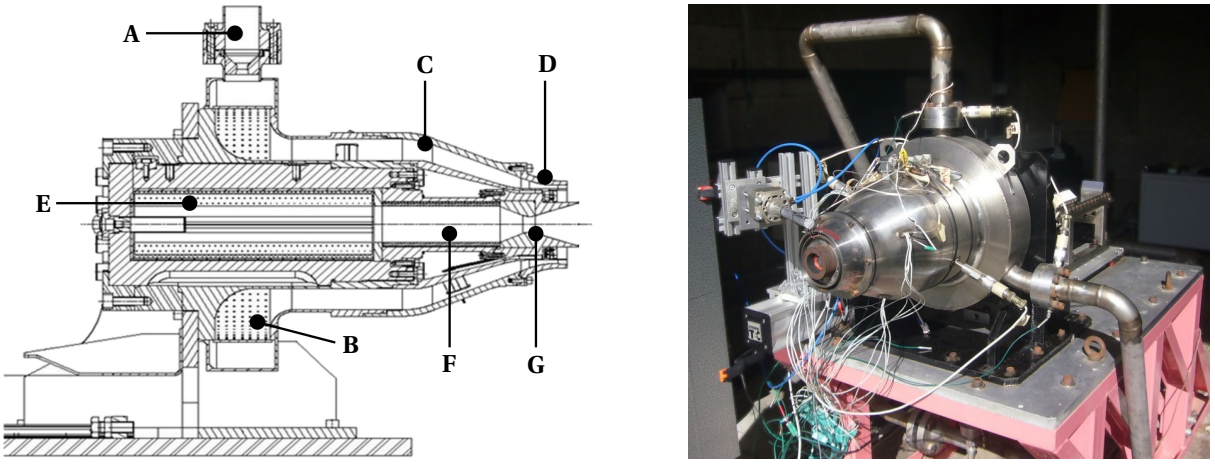

(a) (b)

Figure 1 : (1a) Schematic view and (1b) picture of the LP13 experimental setup.

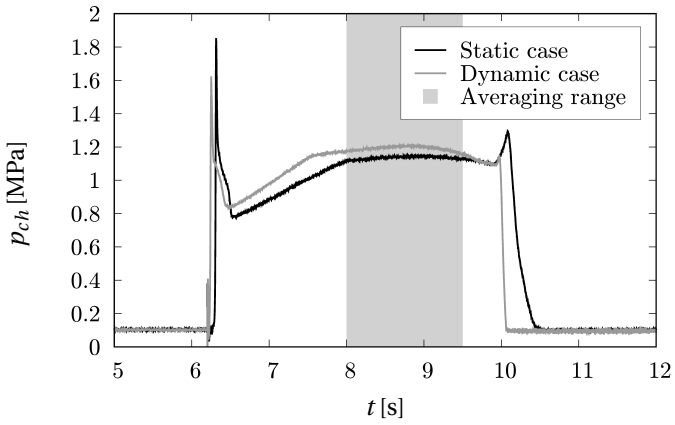

Figure 2 : Chamber pressure over time in the static and dynamic cases.

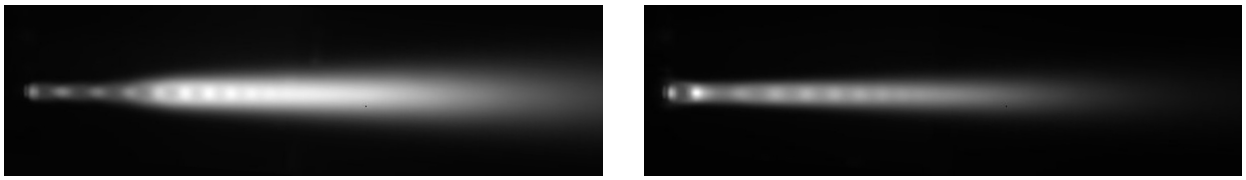

(a) (b)

Figure 3 : Mean contrast radiance field in grayscale obtained from the NOXANT infrared camera measurements in (3a) the static case and (3b) the dynamic case.

Phantom camera (V711-1280×800 pixels) is coupled to a HiCATT intensifier (Lambert Instrument-Gen II) and a UV lens (Sodern-100 mm – f/2.8). It is also equipped with a $\lambda = 310$ nm band pass filter of full width at half maximum FWHM = 5 nm in order to collect only the chemiluminescence signal emitted by the excited hydroxyl radical (OH^*). This signal is a relevant flame position marker below 2800 K [16] and provides more insight into the flame structure. The acquisition frame rate is $f = 600$ Hz and the spatial resolution of the image is 0.32 mm/pixel. This system will be called UV camera in the following.

2.3 Flow conditions

The flow conditions taken as inputs in the corresponding simulations are deduced from the available measurements and zero-dimensional calculations. The air supply for the co-flow provides a total pressure $p_{icf} = 4.5$ bar and a total temperature $T_{icf} = 300$ K. The theoretical Mach number in the exit plane of the co-flow for an isentropic expansion is $M_{cf} = 1.5$.

According to Figure 2, the averaged motor pressure is $p_{ch} = 11.35$ bar in the static case and $p_{ch} = 11.91$ bar in the dynamic case. A thermochemical equilibrium calculation at an intermediate pressure and with a combustion efficiency $\eta = 98.5\,\%$ yields a total chamber temperature $T_{ich} = 2557$ K and a gas composition reported in Table 1. Note that the exhaust mainly contains N_2, H_2O, CO, CO_2 and HCl species. The jet Mach number and temperature on the axis in the exit plane are estimated to $M_j = 2.1$ and $T_j = 1700$ K respectively.

Finally, the ambient air is set to standard conditions, *i.e.* a pressure $p_\infty = 101325$ Pa, a temperature $T_\infty = 298.5$ K and mass fractions $Y_{N_2} = 0.767$ and $Y_{O_2} = 0.233$.

Table 1 : Mass fraction Y_j [−] of the main burnt propellant gases at the thermochemical equilibrium in the solid rocket motor chamber.

Y_{N_2}	Y_{O_2}	Y_O	Y_{H_2}	Y_{H_2O}	Y_H	Y_{OH}	Y_{CO}	Y_{CO_2}	Y_{HCl}	Y_{Cl}	Y_{Cl_2}
0.106192	3.6×10^{-5}	1.9×10^{-5}	0.01285	0.2562	0.000157	0.001314	0.2365	0.1332	0.2493	0.004215	1.7×10^{-5}

3. Numerical modeling

3.1 Flow solver

The axisymmetric compressible Reynold-Averaged Navier-Stokes (RANS) equations are solved with the multi-physics CFD code CEDRE which operates a cell-centered finite-volume method on general unstructured elements [11, 17]. In the context of compressible flows, a mass-weighted Favre averaging is preferred to the standard Reynolds averaging. The specific heat of all transported species is approximated by a 7th order polynomial. Species viscosity is defined according to the Sutherland law. The time integration is performed with an implicit 1st order scheme associated with a Generalized Minimal RESidual (GMRES) method type linear system solver. The reconstruction on cell faces is carried out with a 2nd order k-exact method [18] and the flux is calculated with a Harten-Lax-van Leer-Contact (HLLC) flux-difference splitting scheme [19].

3.2 Turbulence model

A two-equation $k-\omega$ turbulence model with the classical Boussinesq assumption is used in the present simulations. The Shear-Stress Transport (SST) formulation of Menter [20] is adopted with a source term base on vorticity [21]. The Pope correction is implemented in order to take into account round-jet/plane-jet anomaly [22], as well as the Sarkar correction for the compressibility effects [23].

Simulation of supersonic turbulent flows with CEDRE has been widely addressed and validated in the past decades [24]. In particular, the supersonic hot free jet from the MARTEL case [25] has been computed using the same RANS approach and successfully compared to the experimental measurements and a LES reference solution.

3.3 Combustion model

3.3.1 Kinetic model

Within this numerical framework, the afterburning process is modeled by finite rate chemistry. The chemical reactions are described by a 12 species − 17 reactions skeletal kinetic scheme proposed by Troyes *et al.* [13] and recently assessed by Ecker *et al.* [26]. An Arrhenius law is assumed for the reaction rate as

$$\dot{\omega_r} = A_r T^{\eta_r} \exp\left(\frac{-E_{ar}}{RT}\right) \prod_i C_i^{\nu_{r,i}} = K_r(T) \prod_i C_i^{\nu_{r,i}} \tag{1}$$

where C_i is the molar concentration of the reactive species i, $\nu_{r,i}$ the stoichiometric coefficient of species i in reaction r and R the universal gas constant. The Arrhenius parameters A_r, η_r and E_{ar} in the expression of the rate constant K_r are given for each reaction in Table 2, where the branching/recombination/dissociation reactions $r \in [1-8]$ account for the H_2/O_2 combustion, $r \in [9-11]$ for the CO/O_2 combustion and $r \in [12-17]$ for the inhibitor effect of HCl. The contribution of all reactions yields the species production rate as

$$\dot{\omega_j} = \sum_r \nu_{r,j} \dot{\omega_r} \tag{2}$$

The integration of the kinetic model in CEDRE has been verified by comparing the evolution of homogeneous reactors with zero-dimensional simulations performed with a Chemkin solver, analogously to Gueyffier *et al.* [27].

3.3.2 Turbulence-chemistry interaction model

Under the Quasi-Laminar (QL) approximation, the mean reaction rate $\overline{\dot{\omega_r}}$, production rate $\overline{\dot{\omega_j}}$ and heat release $\overline{\dot{\omega_T}}$ are directly deduced from the mean flow variables. However for high-speed turbulent flows, the intermittent behavior of the flow variables and the nonlinearity of Equation 1 makes these averages more difficult to evaluate. The interaction of temperature and composition fluctuations with chemical reactions must be modeled because it may enhance, limit or suppress the afterburning process. This point is particularly crucial with a RANS approach since all turbulent fluctuations are unresolved. The mean production rate can be generalized by the expression

$$\overline{\dot{\omega_j}} = \int_\Psi P(\psi) \dot{\omega_j}(\psi) \mathrm{d}\psi \tag{3}$$

where P is a scalar probability density function (PDF) defined on the associated domain Ψ, and $\psi = [T, Y_j]^T$ the flow variable vector.

Table 2 : List of chemical reactions from Troyes *et al.* [13]. The third body efficiencies are given by Warnatz [28].

No. r	Reaction	A_r [m-mol-s units]	η_r [−]	E_{a_r} [J/mol]	Reference
1	$H + O_2 \rightleftharpoons OH + O$	1.99E+08	0	7.03E+04	[29]
2	$H_2 + O \rightleftharpoons OH + H$	5.12E−02	2.67	2.63E+04	[30]
3	$H_2 + OH \rightleftharpoons H_2O + H$	1.02E+02	1.6	1.38E+04	[30]
4	$OH + OH \rightleftharpoons H_2O + O$	1.51E+03	1.14	4.14E+02	[30]
5	$H + H + M \rightleftharpoons H_2 + M$	8.99E+05	-1	0	[31]
6	$H + OH + M \rightleftharpoons H_2O + M$	2.21E+10	-2	0	[30]
7	$H + O + M \rightleftharpoons OH + M$	4.71E+06	-1	0	[32]
8	$O + O + M \rightleftharpoons O_2 + M$	1.45E+05	-1	0	[28]
9	$CO + OH \rightleftharpoons CO_2 + H$	6.32E+00	1.5	−2.08E+03	[30]
10	$CO + O_2 \rightleftharpoons CO_2 + O$	2.50E+06	0	2.00E+05	[28]
11	$CO + O + M \rightleftharpoons CO_2 + M$	5.00E+00	0	−9.70E+03	[31]
12	$HCl + H \rightleftharpoons H_2 + Cl$	1.69E+07	0	1.73E+04	[33]
13	$Cl_2 + H \rightleftharpoons HCl + Cl$	8.55E+07	0	4.89E+03	[33]
14	$HCl + OH \rightleftharpoons H_2O + Cl$	2.71E+01	1.65	−9.20E+02	[33]
15	$HCl + O \rightleftharpoons OH + Cl$	3.37E−03	2.87	1.47E+04	[33]
16	$Cl + Cl + M \rightleftharpoons Cl_2 + M$	4.68E+02	0	−7.53E+03	[33]
17	$Cl + H + M \rightleftharpoons HCl + M$	7.18E+09	-2	0	[33]

The Partially Stirred Reactor closure (PaSR) is suited to supersonic turbulent combustion [15] and can provide a better description of the afterburning flame. The PaSR model is based on the Eddy Dissipation Concept (EDC) introduced by Magnussen [34]. It relies on the division of each elementary computation volume into a fine-scale structure region, denoted by the superscript $*$, where molecular mixing and chemical reactions occur as in a well-stirred reactor, and a nonreactive surrounding region, denoted by the superscript 0. In this framework, a bimodal PDF is assumed, representing the contribution from both regions, and the mean production rate becomes

$$\overline{\dot{\omega}_j} \approx \gamma^* \dot{\omega}_j(\psi^*) + \left(1-\gamma^*\right)\dot{\omega}_j(\psi^0) \approx \gamma^* \dot{\omega}_j(\psi^*) \tag{4}$$

where γ^* is the fine-scale structure volume fraction. The mass and energy balance equations between the fine-scale structure and the surrounding regions, written for N species, are given as

$$\begin{cases} \overline{\rho}\left(Y_j^* - Y_j^0\right) = \tau_m \dot{\omega}_j(T^*, Y_j^*) \\ \overline{\rho}\sum_{j=1}^N \left(Y_j^* h_j^* - Y_j^0 h_j^0\right) = \tau_m \sum_{j=1}^N h_{j_f} \dot{\omega}_j(T^*, Y_j^*) \end{cases} \tag{5}$$

where h_j and h_{j_f} are respectively the enthalpy and the formation enthalpy of species j, and τ_m a mixing time scale. The system can be closed using the link existing between the regions, expressed as

$$\begin{cases} \tilde{Y}_j = \gamma^* Y_j^* + \left(1-\gamma^*\right) Y_j^0 \\ \tilde{T} = \gamma^* T^* + \left(1-\gamma^*\right) T^0 \end{cases} \tag{6}$$

where the $\sim$ accent stands for the Favre averaging. The mean flow variables $\tilde{Y}_j$ and $\tilde{T}$ are provided by the RANS solver.

The PaSR differs from the EDC on the definition of γ^* and τ_m. The expressions retained by Moule *et al.* [15] are chosen here and are given as

$$\gamma^* = \frac{\tau_c}{\tau_c + \tau_m} \tag{7}$$

$$\tau_m = \sqrt{\tau_\kappa \tau_l} \tag{8}$$

in which τ_c is a chemical time scale, $\tau_\kappa = (\nu/(C_\mu k\omega))^{1/2}$ the Kolmogorov time scale and $\tau_l = k/\epsilon = 1/(C_\mu \omega)$ the turbulence integral time scale, with ν the laminar viscosity, k the turbulent kinetic energy, ϵ the turbulent kinetic energy dissipation rate, ω the turbulence specific dissipation and $C_\mu = 0.09$ a standard parameter of the turbulence model.

Under certain conditions, the well-stirred reactor in the fine-scale structure region can admit multiple solutions [35] : a frozen or weak-reaction solution, an intense-reaction solution and an intermediate non-physical solution. The convergence towards a particular solution is then determined by the reactor past history. In practice in this study, the system formed by Equations 5 and 6 is solved by a Newton-Raphson algorithm and the convergence towards a physical solution is not ensured. In case of non-convergence, the intense-reaction solution is enforced. In parallel, an additional procedure is applied to predict the reactor extinction, *i.e.* the frozen solution, as described in Section 3.3.3.

Computation time can be saved by preventing the PaSR procedure from operating outside the flame region in the jet mixing layer. An allowable range of mixture fraction Z between the burnt propellant gases and the surrounding air is implemented for that purpose, as $Z_{min} \leq Z \leq Z_{max}$. Z is a passive scalar defined as

$$Z = \frac{Y_{C+H} - (Y_{C+H})_{air}}{(Y_{C+H})_{jet} - (Y_{C+H})_{air}} \tag{9}$$

where Y_{C+H} is the cumulative mass fraction of carbon and hydrogen atoms. The bounds are set to $Z_{min} = 0.02$ and $Z_{max} = 0.98$. A volume fraction $\gamma^* = 0$ is prescribed for $Z < Z_{min}$ but $\gamma^* = 1$ for $Z > Z_{max}$, which enables the kinetic model to apply inside the nozzle and the jet potential core during expansion.

A model for the characteristic chemical time scale τ_c must finally be specified. Several expression are proposed in the literature, such as the ratio of the flame thickness and the propagation velocity for a one-dimensional laminar premixed flame [15], or the inverse of the species production rates [36] for example. The idea of linking the chemical time scale to reaction rates [37, 38] is preferred here. The present model focuses on the branching reactions of the OH radical with H_2 ($r = 3$) and CO ($r = 9$) which are essential in the afterburning ignition process. The chemical time scale is finally modeled by a geometric mean as

$$\tau_c = \sqrt{\tau_{r=3}\tau_{r=9}} \tag{10}$$

where the reaction time scale τ_r is calculated as

$$\tau_r = \frac{\prod_i C_i^{\frac{\nu_{r,i}}{\sum_i \nu_{r,i}}}}{\dot{\omega_r}} = \left(K_r(T) \prod_i C_i^{\nu_{r,i} - \frac{\nu_{r,i}}{\sum_i \nu_{r,i}}} \right)^{-1} \tag{11}$$

A validation study is conducted to check the relevance of this model, especially the choice to rely on branching reactions $r \in [3,9]$. The main results are reported in Figure 4. Zero-dimensional simulations are carried out with a Chemkin solver to calculate induction time of homogeneous reactors at prescribed pressure, as illustrated in Figure 4a. The reactor initial conditions (p_0, T_0, Y_j) are taken from various flow states found in the jet mixing layer region in simulations of the LP13 configuration under the QL approximation, in both static and dynamic cases. Multiple definitions of the induction time are possible, as the time of maximum temperature derivative dT/dt or the time required to reach a specific temperature increase rate $(T - T_0)/(T_1 - T_0)$. The time corresponding to increases of 2 % and 5 %, respectively denoted $\tau_{\Delta T=2\%}$ and $\tau_{\Delta T=5\%}$, are computed then compared to τ_c as a function of Z in Figure 4b. The time of maximum dT/dt gives similar values to those of $\tau_{\Delta T=2\%}$. A good agreement is found for mixture fractions $Z > 0.3$ in terms of order of magnitude and variation trends with Z, indicating that the model for τ_c successfully provides a relevant chemical time scale in that range. For $0.15 < Z < 0.3$, τ_c appears overestimated. Below $Z = 0.15$, the temperature elevation in the homogeneous reactors is not significant enough to calculate a relevant induction time, which explains the abnormal drop. The model is satisfactory knowing that the maximum heat release levels (not plotted) are found at $Z = 0.55$ in the static case and $Z = 0.5$ in the dynamic case.

3.3.3 Extinction model

According to Calhoon [8], two plausible mechanisms can explain the afterburning shutdown observed in supersonic hot exhaust plume. The first one is the competition between the heat release rate due to the afterburning and the cooling due to the turbulence mixing with ambient air, and is implicitly taken into account using a finite rate chemistry model. The second one occurs when the strain rate between turbulent structures of the mixing layer becomes too large, inducing local extinction of the flame.

This latest phenomenon is strongly linked to the intermittent behavior of the flow and must be explicitly modeled in a RANS framework by enforcing the frozen solution if an extinction criterion is satisfied. The strain rate being inversely proportional to a turbulence time scale, the criterion can be specified as a comparison between a turbulence time scale and an extinction chemical time scale [8, 35]. The choice of the relevant time scales remains debated in the literature. In the present work, the turbulence time scale is set as the local turbulence integral

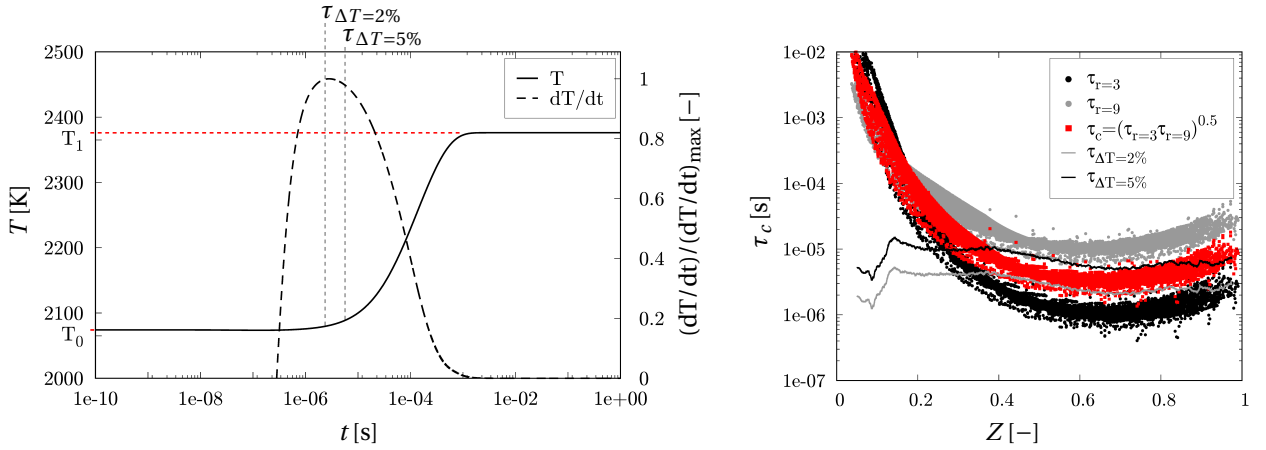

(a) (b)

Figure 4 : Validation study for the chemical time scale model ; (4a) example of induction time computation from the temperature variation over time in a zero-dimensional homogeneous reactor ; (4b) comparison between the mean induction time $\tau_{\Delta T}$ and the modeled chemical times τ_c scatter plot as a function of the mixture fraction Z.

time τ_l to model the strain effect between large-scale structures as proposed by Miake-Lye and Hammer [39]. The extinction time is modeled as a quantity depending on the local chemical time τ_c previously introduced.

A calibration constant denoted C_{ext} is finally introduced by Calhoon [8] to define the extinction criterion such as $\tau_l < C_{ext}\tau_c$. This constant can be seen as a critical Damköhler number and is intuitively expected in the order of magnitude of the unity. It is taken equal to 3 to match the flame lift-off distance observed in the LP13 experiment in the static case (see Section 5), which is close to the value of 2.43 calculated by Sloan and Sturgess [35].

This simple extinction model is integrated to the PaSR framework following a procedure adapted from that proposed by Sloan and Sturgess [35], and described by the flowchart in Figure 5. It provides a binary switch for the afterburning process such as if the extinction criterion is met, γ^* is set to 0 and the PaSR resolution is bypassed, which is equivalent to a pure mixing without chemical reaction.

4. Case simulation

4.1 Computational setup

The RANS simulations of the LP13 configuration are carried out with CEDRE on a 2D axisymmetric numerical domain represented in Figure 6. It extends over $164.5r_{nzl}$ in the axial direction and up to $45r_{nzl}$ in the radial direction, with $r_{nzl} = 20$ mm the motor nozzle exit radius. The origin of the coordinate system is located at the intersection of the co-flow exit plane with the symmetry axis. At $x = 0$, the annular channel has an outer radius of $r_{cf} = 2.85r_{nzl}$ and an inner radius of $r_{cf} - h_{cf} = 2.5r_{nzl}$. The motor exit plane is positioned at $x_{nzl} = 0.75r_{nzl}$. The flow conditions given in Section 2.3 are prescribed at the annular inlet for the air co-flow, at the motor inlet for the burnt propellant gases and at the external boundaries for the ambient air at rest.

An unstructured mesh is created consisting in quad layers at most of the walls and triangle cells elsewhere. A particular attention is paid to the refinement of the nozzle wall, the annular channel walls and the motor base region.

4.2 Grid convergence

A grid convergence study is firstly conducted without the PaSR and extinction models, *i.e.* under the QL approximation, in the dynamic case. Simulations are run on seven gradually refined grids, with a time step $\Delta t = 1 \times 10^{-7}$ s, until the steady state is reached. The refinement is performed by applying a factor on the cell size over the entire mesh. The resulting solutions are compared to a reference field obtained on a grid composed of $n_{cell\,ref} = 1.7 \times 10^6$ elements.

A metric defined as the mean relative error of a variable x on the $Z = 0.5$ isoline is calculated for the pressure, temperature, velocity, turbulent kinetic energy and heat release, for each grid. It should be noticed that the recirculating flow in the motor base region is the most sensitive feature to the mesh refinement, but this mixture fraction

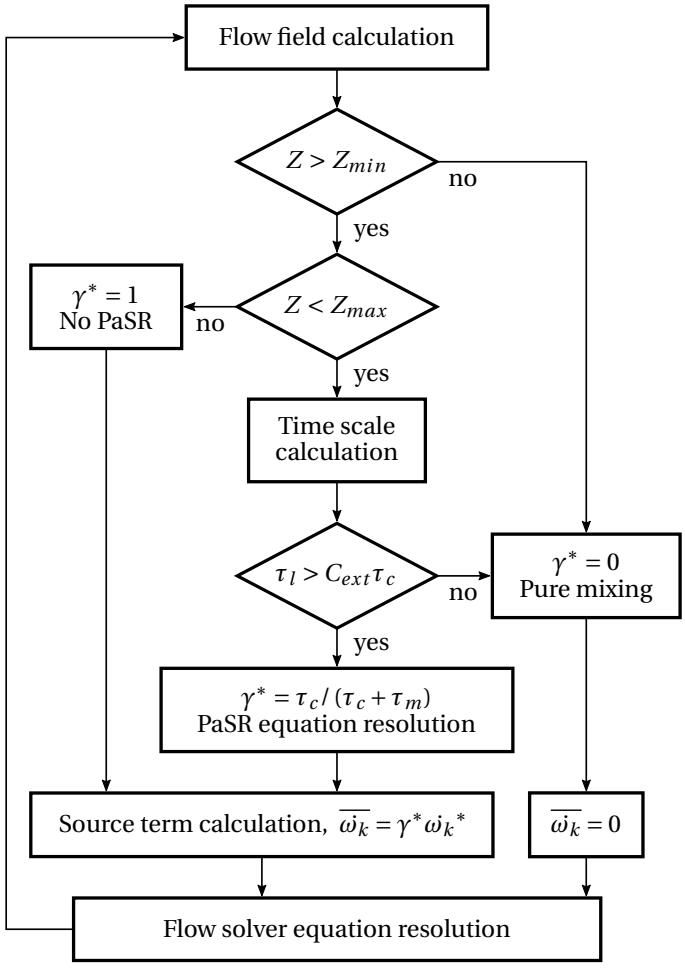

Figure 5 : Flowchart for the flow solution calculation procedure using the PaSR model and the extinction model (adapted from Sloan and Sturgess [35]).

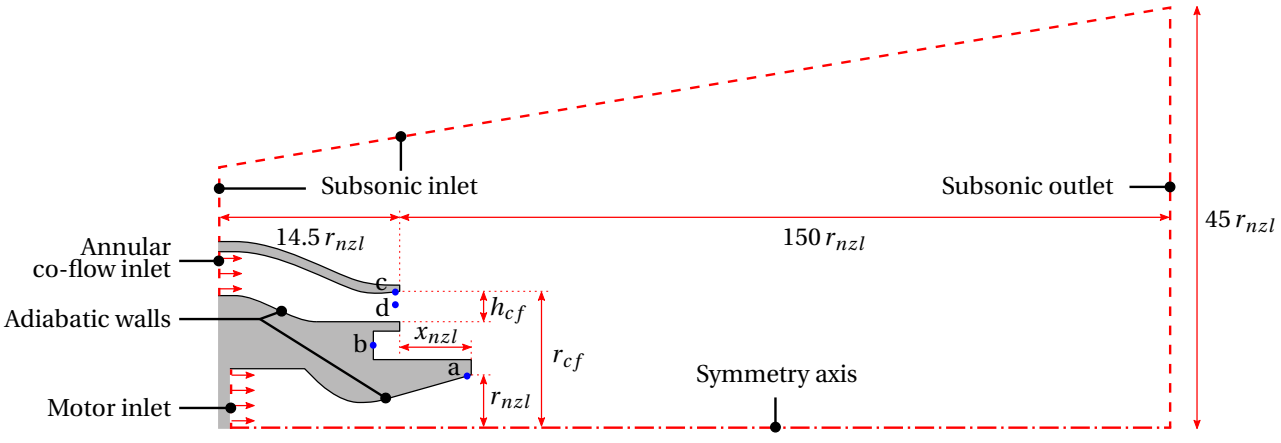

Figure 6 : Schematic view of the computational domain and boundary conditions.

isoline is chosen due to its central location inside the afterburning flame. All quantities exhibit a gradual convergence. The highest errors are found for the heat release and an error lower than 2 % is achieved only on the very fine and ultra fine grids, respectively denoted VFG and UFG. A trade-off between the number of grid elements and the accuracy is also sought because of the high computational cost of the combustion model. Consequently, the VFG grid, composed of $n_{cell} = 551 \times 10^3$ elements, is considered satisfactory and is therefore used in the following.

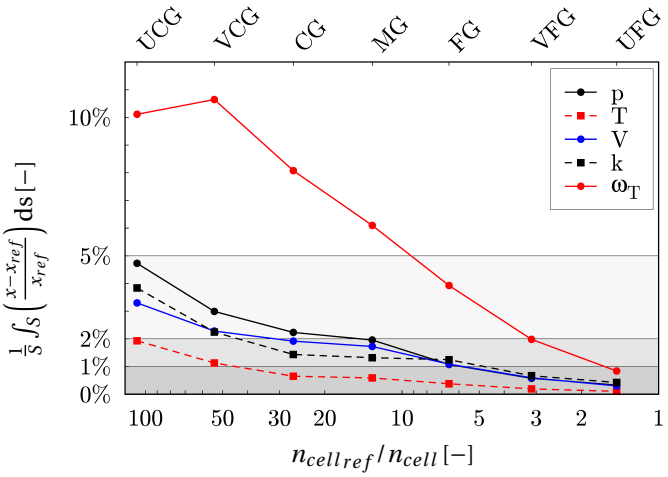

Figure 7 : Grid convergence study ; mean relative error on pressure p, temperature T, velocity V, turbulent kinetic energy k and heat release ω_T, along the $Z = 0.5$ isoline of curvilinear abscissa s.

4.3 Flow solution validation

The pressure field from the flow solution converged on the VFG grid is confronted to experimental measurements at key locations in Table 3. A total pressure measurement operated with a Pitot tube inside the annular channel slightly upstream of the exit plane gives access to a local Mach number of the co-flow. The simulation agrees well with the experimental data in both static and dynamic cases, which adds credit to the numerical results. The low-pressure found for p_{base} at the motor base in the dynamic case is induced by the supersonic co-flow overexpansion. The value is underestimated by about 50 mbar in the simulation but the trend compared to the static case is recovered.

Simulations using the PaSR model alone, as well as using both the PaSR and the extinction models, are then conducted. Only minor differences are noticed on the pressure fields (not shown). No hysteresis is detected when the new solutions are computed from a "cold" frozen initial solution, *i.e.* without any chemical reaction, or a "hot" QL initial solution. This phenomena could have been expected since the local behavior of the PaSR and extinction models can depend on the upstream flow state.

Table 3 : Comparison of measured and simulated co-flow Mach number and differential pressure value at key locations marked on Figure 6.

Quantity	Probe location	Static case		Dynamic case	
		Experiment	Simulation	Experiment	Simulation
$p_{nzl} - p_\infty$ [mbar]	nozzle wall at $x = x_{nzl} - 0.14 r_{nzl}$ marker **a** on Figure 6	$+427 \pm 12$	$+478$	$+550 \pm 18$	$+555$
$p_{base} - p_\infty$ [mbar]	motor base marker **b** on Figure 6	$+0 \pm 5$	$+0$	-150 ± 8	-198
$p_{cf} - p_\infty$ [mbar]	co-flow wall at $x = -0.2 r_{nzl}$ marker **c** on Figure 6	N/A	N/A	$+333 \pm 4$	$+343$
M_{cf} [−]	co-flow at $x = -0.2 r_{nzl}$ marker **d** on Figure 6	N/A	N/A	1.46 ± 0.1	1.42

5. Results and discussion

5.1 Effect on the flow structure

The effect of the surrounding air co-flow on the exhaust jet is illustrated by the Mach number fields and the streamlines depicted in Figure 8. In the static case, the supersonic jet of burnt propellant gases is overexpanded and presents classical shock cell structures. The convergence of the ambient air streamlines towards the jet mixing layer is due to the jet suction effect.

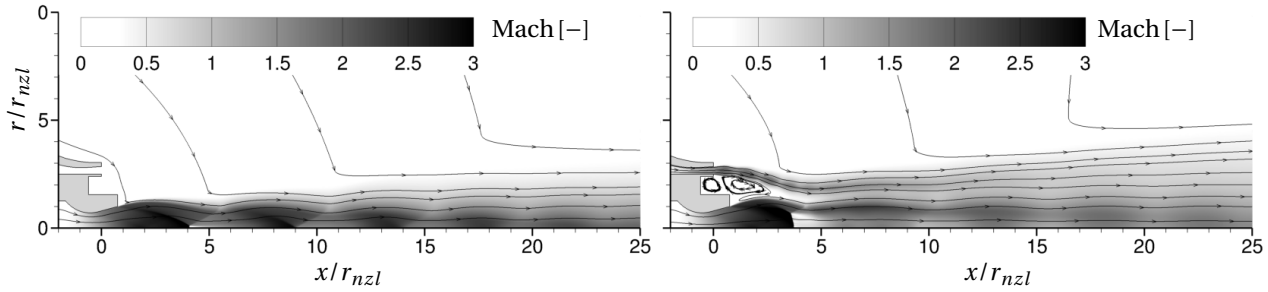

(a) (b)

Figure 8 : Simulated Mach number fields and streamlines in (8a) the static case and (8b) the dynamic case.

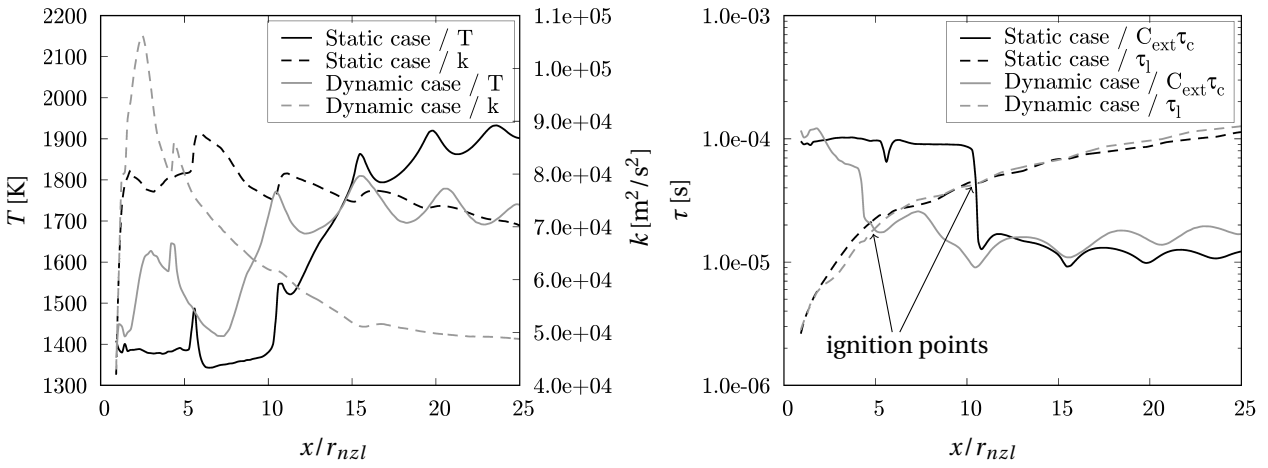

(a) (b)

Figure 9 : Simulated profiles of (9a) temperature T and turbulent kinetic energy k, and (9b) extinction time scale $C_{ext}\tau_c$ and turbulent time scale τ_l, at the radial location of maximum k inside the mixing layer.

In the dynamic case, the supersonic co-flow shows small annular shock cells. The low-pressure induced by the co-flow amplify the jet overexpansion and a large Mach disk appears at $x = 3.75r_{nzl}$. As mentioned before, a recirculating flow develops in the motor base region. Two annular recirculation bubbles are visible in Figure 8b, and the largest one is oriented clockwise on the image. It locally increases the velocity differential in the mixing layer along the first shock cell and consequently raises the maximum of turbulence kinetic energy k as plotted in Figure 9a. Downstream, the co-flow merges with the jet mixing layer, decreasing the velocity differential as well as k. Hot gas from the jet is also entrained upstream by the recirculation, which quickly heats up the mixing layer downstream of the exit while it remains colder in the static case. It translates into shorter chemical and extinction time scales along the first two shock cells in the dynamic case as shown in Figure 9b.

5.2 Effect on the afterburning

The surrounding flow also deeply affects the afterburning process as highlighted by the camera measurements. The radiance fields acquired by the NOXANT infrared camera and displayed in Figure 3 reveal low emission levels along the first two shock cells, then a larger and more intense emission zone downstream in the static case compared to the dynamic case. The OH^* chemiluminescence emission fields measured by the UV camera and displayed in Figure 10 exhibit a non reactive zone in the range $0 \leqslant x \lesssim 10r_{nzl}$ that confirms it can be attributed to a flame lift-off phenomenon occurring only in the static case (Figure 10a). Conversely, the recirculating flow in the dynamic case acts as a flameholder and the flame is attached (Figure 10b). Note that the temperature immediately downstream of the Mach disk is expected to reach levels in the order of the total temperature T_{ich}. Although below 2800 K [16], the associated radiation is pure thermal excitation and can be ignored for the flame topology analysis.

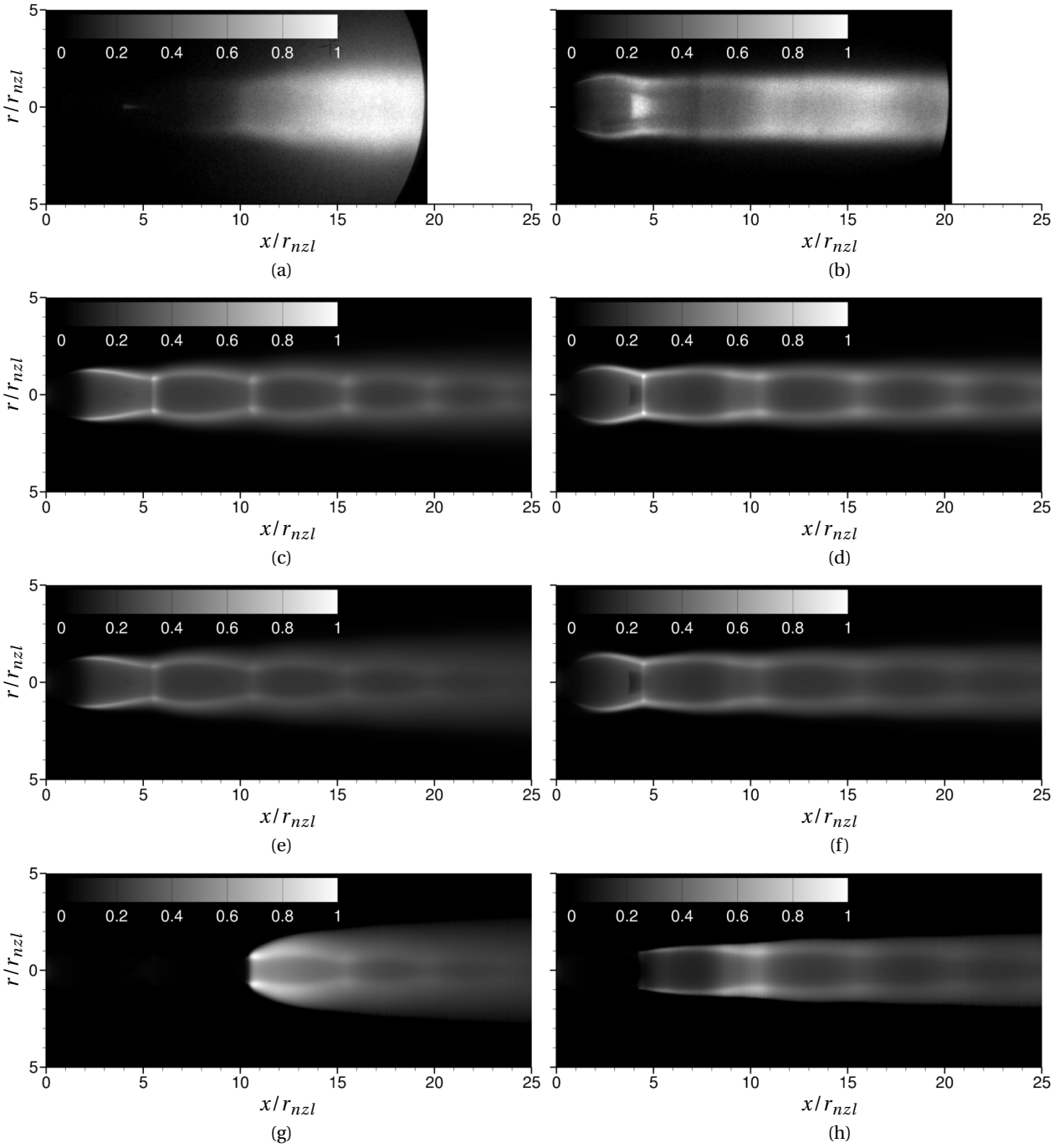

Figure 10 : Comparison of the normalized level of mean OH^* chemiluminescence emission measured by the UV camera with the simulated normalized level of Abel transform of mean heat release ω_T in (left) the static case and (right) the dynamic case ; (10a)(10b) camera measurements ; (10c)(10d) simulations under quasi-laminar approximation ; (10e)(10f) simulations with PaSR model alone ; (10g)(10h) simulations with PaSR and extinction models.

The OH^* emission is put in parallel with the simulated heat release in Figure 10. This quantity is commonly used as flame marker in simulations [14, 15, 36]. An overlay with the flame index (not plotted), also known as the Takeno index [37], shows negative values everywhere the heat release in the mixing layer is higher or equal to 1% of its maximum. It indicates a pure diffusion combustion regime in both static and dynamic cases.

The heat release fields depicted in Figures 10c to 10h are convoluted in the azimuthal direction *via* an Abel transform and all levels are normalized by the same reference value. A direct comparison between the experimental and numerical normalized levels is not relevant but the fields bring quantitative information on the jet and the

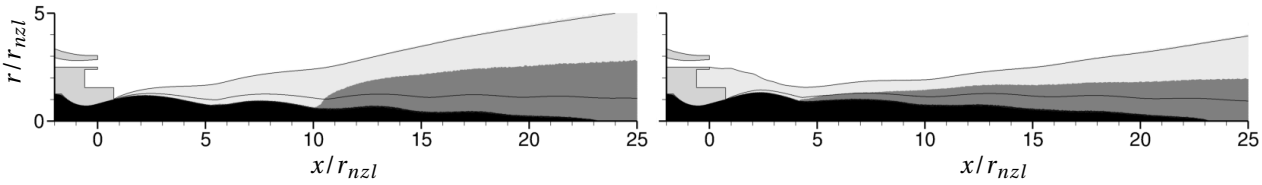

(a) (b)

Figure 11 : Contour plot of the extinction model switch regions, including isolines $Z \in [Z_{min}, 0.5, Z_{max}]$, in (11a) the static case and (11b) the dynamic case ; black region : $Z > Z_{max}$ and $\gamma^* = 1$; dark grey region : PaSR resolution ; light grey region : extinction and $\gamma^* = 0$; white region : $Z < Z_{min}$ and $\gamma^* = 0$.

flame structures. It is firstly observed that the QL approach (Figures 10c and 10d) fails to adequately predict the afterburning flame topology. The flame lift-off is indeed not captured in the static case and the location of maximum heat release is not positioned in the expected zone of maximum combustion intensity in both cases. However, the mixing layer shape and the shock positions are finely reproduced, which is particularly visible in the dynamic case. The simulations with the PaSR model alone (Figures 10e and 10f) do not improve the flame topology and only result in a limited overall reduction of the heat release with respect to the QL simulations.

On the other hand, the simulations with the extinction model (Figures 10g and 10h) yields significant changes. In the static case, the flame lift-off is captured as well as the spreading in the radial direction downstream of the ignition point at $x = 10.75 r_{nzl}$, but the highest heat release levels are found near this point while the zone of maximum combustion intensity is located in the range $15 r_{nzl} \lesssim x \lesssim 20 r_{nzl}$ in the experiment. In the dynamic case, the ignition point moves upstream but the model still predicts an unexpected small extinction region along the first shock cell. Nevertheless, the heat release levels are increased downstream as in the experiment.

The simulated flame behavior is correlated with the extinction model switch regions represented in Figure 11. The light grey region corresponds to cells where the extinction criterion is satisfied and the dark grey region to cells where the PaSR model is allowed to operate. It emphasizes that the ignition points are located at the crossing points between the mixing layer and the reflected shocks that helps to stabilize the flame. The difference in lift-off distance can be explained by the changes in the mixing layer state between the static and the dynamic cases as discussed in Section 5.1. An analysis of the turbulence time scale τ_l inside the mixing layer as given in Figure 9b reveals little discrepancies between the static and dynamic cases, suggesting that the extinction model is mainly driven by the variation of the chemical time scale τ_c. In other words, the colder mixing layer implies slower chemical reactions that favor the extinction and the ignition point moves downstream in the static case. Accounting for the local variations of composition and temperature in the model for τ_c as it is done here seems therefore necessary.

From a general point of view, the simulations with the extinction model provide better trends for the flame topology, especially for the lift-off situation and despite the fact it fails to predict the attached flame. This difficulty could be due to uncertainties on the case inputs, to a lack of numerical accuracy in reproducing the recirculating flow or the initial mixing layer state, but also to a limitation of the extinction model because of its simplicity as suggested by Sloan and Sturgess [35].

The consequences of the turbulence-chemistry interaction modeling on the temperature distribution can be seen on the fields in Figure 12. The temperature profiles along the jet axis and the jet radius at $x = 33 r_{nzl}$ are extracted from these fields and plotted in Figure 13. As similarly obtained by Calhoon [8], the PaSR and extinction models induce an important plume cooling compared to the QL simulations. The static case shows a maximal temperature drop of about 200 K on the axis at $x = 33 r_{nzl}$ that increases to 260 K in the dynamic case. The recirculating flow in the motor base region also experiences a global cooling of 200 K, which is probably overestimated because of the unexpected lifted flame that limits the temperature elevation in the mixing layer along the first shock cell. These results presume a substantial impact on the heat fluxes on the motor base and the plume infrared radiation.

6. Conclusion

The numerical simulation of the afterburning plume exhausting from a solid propellant rocket motor, corresponding to a ground experiment, has been undertaken with a Reynolds-averaged Navier-Stokes solver in this study. A Partially Stirred Reactor (PaSR) model and an extinction model have been adapted to this numerical framework. The influence of the supersonic surrounding flow generated by an annular channel that mimics a flight effect has been examined by comparing results in the static and dynamic cases. Experimental evidences show an afterburn-

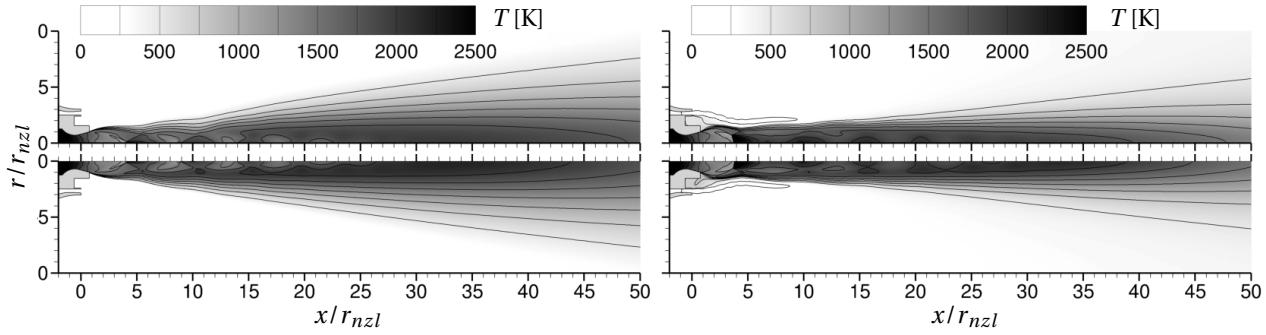

Figure 12 : Simulated temperature fields with (top) PaSR and extinction models and (bottom) under quasi-laminar approximation in (12a) the static case and (12b) the dynamic case.

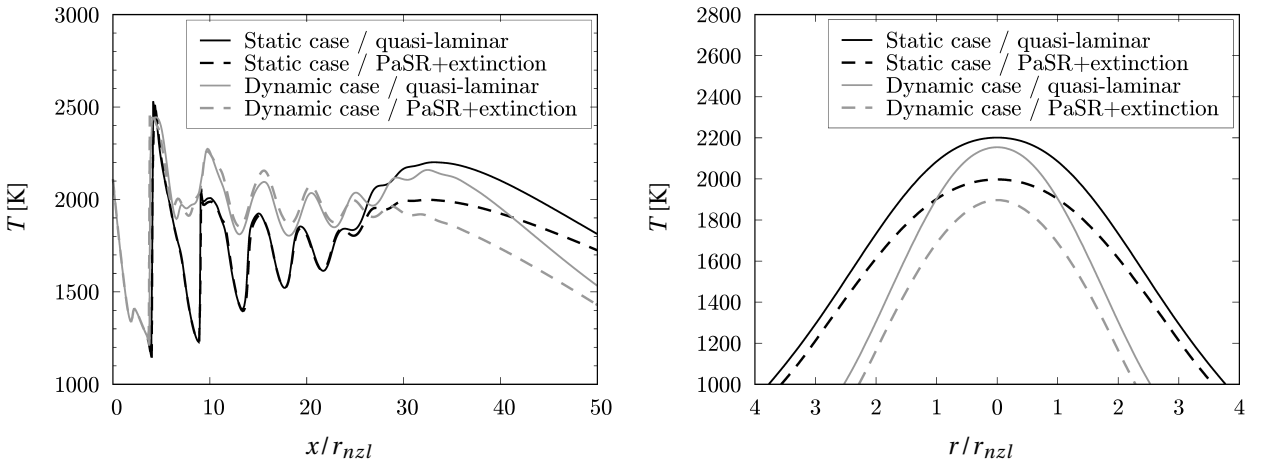

Figure 13 : Simulated temperature profiles along (13a) the jet axis and (13b) the jet radius at $x = 33 r_{nzl}$.

ing flame lift-off in the static case. The simulated heat release fields obtained using the quasi-laminar approximation, the PaSR model alone and both the PaSR and extinction models indicate that the PaSR yields a limited reduction of the combustion intensity while only the extinction model allows to capture the lift-off behavior. This is achieved in particular thanks to a model accounting for the local composition and temperature for the evaluation of the chemical time scale. These findings support that a specific turbulence-chemistry interaction modeling, often neglected in the literature focusing on the heat fluxes or the plume signature assessment, is needed for such applications.

The simulations with the extinction model better reproduce the afterburning flame overall topology, but it fails to predict the attached flame in the dynamic case. Additional investigations are required to clarify this issue that could be due to uncertainties on the case inputs, numerical inaccuracies but also to a predictivity limitation of the model because its simplicity.

Further quantitative comparisons between the simulations and the infrared camera measurements will be performed by applying a dedicated radiative transfer solver as described by Rialland *et al.* [12]. The effect of the turbulence-chemistry interaction modeling on the plume signature, as well as the contribution of soot particles, will be evaluated. An application of the present numerical methodology to a test case such as the Black Brant sounding rocket in realistic flight conditions [2] could also be considered for extended validation purposes.

Acknowledgments

The authors would like to thank the ONERA's scientific direction and the French Procurement Agency for Armament (DGA) for funding and supporting the present work.

References

[1] F. Simmons. *Rocket Exhaust Plume Phenomenology*. The Aerospace Press, American Institute of Aeronautics and Astronautics, 2000. ISBN: 978-1884989087. DOI: 10.2514/4.989087.

[2] V. Rialland, A. Guy, D. Gueyffier, P. Perez, A. Roblin, and T. Smithson. "Infrared signature modelling of a rocket jet plume - comparison with flight measurements". In : *Journal of Physics: Conference Series* 676.1 (2016), p. 012020. DOI: 10.1088/1742-6596/676/1/012020.

[3] Q. Binauld, J.-M. Lamet, L. Tessé, P. Rivière, and A. Soufiani. "Numerical simulation of radiation in high altitude solid propellant rocket plumes". In : *Acta Astronautica* 158 (2019), pp. 351–360. DOI: 10.1016/j.actaastro.2018.05.041.

[4] A. Alexeenko, N. Gimelshein, D. Levin, R. Collins, R. Rao, G. Candler, S. Gimelshein, J. Hong, and T. Schilling. "Modeling of Flow and Radiation in the Atlas Plume". In : *Journal of Thermophysics and Heat Transfer* 16.1 (2002), pp. 50–57. DOI: 10.2514/2.6651.

[5] Z. Liu, Q. Ye, F. Ding, Y. Xu, and X. Han. "Study on the Influence of Flight Altitude on the Rocket Plume Radiation Enhancement Effect Caused by Afterburning". In : *International Journal of Aeronautical and Space Sciences* 22.5 (2021), pp. 1019–1030. DOI: 10.1007/s42405-021-00376-w.

[6] R. Stowe, S. Ringuette, P. Fournier, T. Smithson, R. Pimentel, D. Alexander, and R. Link. "Effect of Flight and Motor Operating Conditions on IR Signature Predictions of Rocket Exhaust Plumes". In : *International Journal of Energetic Materials and Chemical Propulsion* 14.1 (2015), pp. 29–56. DOI: 10/kdp9.

[7] Q. Niu, Z. ZHe, and S. Dong. "IR radiation characteristics of rocket exhaust plumes under varying motor operating conditions". In : *Chinese Journal of Aeronautics* 30.3 (2017), pp. 1101–1114. DOI: 10.1016/j.cja.2017.04.003.

[8] W. Calhoon. "Computational Assessment of Afterburning Cessation Mechanisms in Fuel-Rich Rocket Exhaust Plumes". In : *Journal of Propulsion and Power* 17.1 (2001), pp. 111–119. DOI: 10.2514/2.5715.

[9] W. Calhoon and D. Kenzakowski. "Assessment of Turbulence-Chemistry Interactions in Missile Exhaust Plume Signature Analysis". In : *Journal of Spacecraft and Rockets* 40.5 (2003), pp. 694–695. DOI: 10.2514/2.6895.

[10] L. Pascal, P. Reulet, J. Anthoine, J. Dupays, and P. Prévot. "Development of a test facility for investigating the solid rocket motor base region in representative external flow conditions". In : *Space Propulsion 2016*. SP2016-3125233. Roma, Italy, 2016.

[11] Y. Fabignon, J. Anthoine, D. Davidenko, R. Devillers, J. Dupays, D. Gueyffier, J. Hijlkema, N. Lupoglazoff, J.-M. Lamet, L. Tessé, et al. "Recent Advances in Research on Solid Rocket Propulsion". In : *Aerospace Lab Journal* 11 (2016), AL11–13. DOI: 10.12762/2016.AL11-13.

[12] V. Rialland, S. Langlois, R. Domel, S. Rommeluere, J. Aubrée, A. Langenais, and C. Lavigne. "Static versus Dynamic Plume Infrared Signature Measurements and Simulations". In : *15th International conference on Target and Background Modeling & Simulation*. Bagnères-de-Bigorre, France, 2022.

[13] J. Troyes, I. Dubois, V. Borie, and A. Boischot. "Multi-phase reactive numerical simulations of a model solid rocket motor exhaust jet". In : *42nd AIAA / ASME / SAE / ASEE Joint Propulsion Conference and Exhibit*. 2006-106. Sacramento, CA, USA, 2006. DOI: 10.2514/6.2006-4414.

[14] V. Sabel'nikov and F. Fureby. "LES combustion modeling for high Re flames using a multi-phase analogy". In : *Combustion and Flame* 160.1 (2013), pp. 83–96. DOI: 10.1016/j.combustflame.2012.09.008.

[15] Y. Moule, V. Sabel'nikov, A. Mura, and M. Smart. "Computational Fluid Dynamics Investigation of a Mach 12 Scramjet Engine". In : *Journal of Propulsion and Power* 30.2 (2014), pp. 461–473. DOI: 10.2514/1.B34992.

[16] T. Kathrotia, M. Fikri, M. Bozkurt, M. Hartmann, U. Riedel, and C. Schulz. "Study of the H+O+M reaction forming OH∗: Kinetics of OH∗ chemiluminescence in hydrogen combustion systems". In : *Combustion and Flame* 157.7 (2010), pp. 1261–1273. DOI: 10.1016/j.combustflame.2010.04.003.

[17] A. Refloch, B. Courbet, A. Murrone, P. Villedieu, C. Laurent, P. Gilbank, J. Troyes, L. Tessé, G. Chaineray, J.-B. Dargaud, et al. "CEDRE Software". In : *Aerospace Lab Journal* 2 (2011), AL02–11.

[18] F. Haider, B. Courbet, and J.-P. Croisille. "A high-order interpolation for the finite volume method: The Coupled Least Squares reconstruction". In : *Computers & Fluids* 176 (2018), pp. 20–39. DOI: 10.1016/j.compfluid.2018.09.009.

[19] E. Toro, M. Spruce, and W. Speares. "Restoration of the Contact Surface in the HLL-Riemann Solver". In : *Shock Waves* 4.1 (1994), pp. 25–34. DOI: 10.1007/BF01414629.

[20] F. Menter, M. Kuntz, and R. Langtry. “Ten Years of Industrial Experience with the SST Turbulence Model”. In : *Turbulence, Heat and Mass Transfer*. Vol. 4. Antalya, Turkey, 2003, pp. 625–632. ISBN: 1567001963.

[21] F. Menter. *Improved two-equation k-omega turbulence models for aerodynamic flows*. Technical Memorandum 103975. NASA, 1992.

[22] S. Pope. “An explanation of the turbulent round-jet/plane-jet anomaly”. In : *AIAA Journal* 16.3 (1978), pp. 279–281. DOI: 10.2514/3.7521.

[23] S. Sarkar. “The pressure-dilatation correlation in compressible flows”. In : *Physics of Fluids A: Fluid Dynamics* 4.12 (1992), pp. 2674–2682. DOI: 10.1063/1.858454.

[24] D. Scherrer, F. Chedevergne, P. Grenard, J. Troyes, A. Murrone, E. Montreuil, F. Vuillot, N. Lupoglazoff, M. Huet, B. Sainte-Rose, et al. “Recent CEDRE Applications”. In : *Aerospace Lab Journal* 2 (2011), AL02–13.

[25] A. Langenais, F. Vuillot, J. Troyes, and C. Bailly. “Accurate simulation of the noise generated by a hot supersonic jet including turbulence tripping and nonlinear acoustic propagation”. In : *Physics of Fluids* 31.1 (2019), p. 016105. DOI: 10.1063/1.5050905.

[26] T. Ecker, S. Karl, and K. Hannemann. “Combustion Modeling in Solid Rocket Motor Plumes”. In : *8^{th} European Conference for Aeronautics and Aerospace Sciences*. Madrid, Spain, 2019. DOI: 10.13009/EUCASS2019-79.

[27] D. Gueyffier, B. Fromentin-Denoziere, J. Simon, A. Merlen, and V. Giovangigli. “Numerical Simulation of Ionized Rocket Plumes”. In : *Journal of Thermophysics and Heat Transfer* 28.2 (2014), pp. 218–225. DOI: 10.2514/1.T4239.

[28] J. Warnatz. “Rate Coefficients in the C/H/O System”. In : *Combustion Chemistry*. 1984, pp. 197–360. DOI: 10.1007/978-1-4684-0186-8_5.

[29] D. Baulch, C. Cobos, R. Cox, C. Esser, P. Frank, Th. Just, J. Kerr, M. Pilling, J. Troe, R. Walker, et al. “Evaluated Kinetic Data for Combustion Modelling”. In : *Journal of Physical and Chemical Reference Data* 21.3 (1992), pp. 411–734. DOI: 10.1063/1.555908.

[30] D. Baulch, C. Cobos, R. Cox, C. Esser, P. Frank, Th. Just, J. Kerr, M. Pilling, J. Troe, R. Walker, et al. “Evaluated Kinetic Data for Combustion Modeling. Supplement I”. In : *Journal of Physical and Chemical Reference Data* 23.6 (1994), pp. 847–848. DOI: 10.1063/1.555953.

[31] U. Maas and J. Warnatz. “Ignition processes in carbon-monoxide-hydrogen-oxygen mixtures”. In : *Symposium (International) on Combustion* 22.1 (1989), pp. 1695–1704. DOI: 10.1016/S0082-0784(89)80182-1.

[32] W. Tsang and R. Hampson. “Chemical Kinetic Data Base for Combustion Chemistry. Part I. Methane and Related Compounds”. In : *Journal of Physical and Chemical Reference Data* 15.3 (1986), pp. 1087–1279. DOI: 10.1063/1.555759.

[33] J. Roesler, R. Yetter, and F. Dryer. “Kinetic interactions of CO, NOx, and HCI emissions in postcombustion gases”. In : *Combustion and Flame* 100.3 (1995), pp. 495–504. DOI: 10.1016/0010-2180(94)00228-K.

[34] B. Magnussen. “The Eddy Dissipation Concept - A Bridge Between Science and Technology”. In : *ECCOMAS Thematic Conference on Computational Combustion*. Lisbon, Portugal, 2005.

[35] D. Sloan and G. Sturgess. “Modeling of Local Extinction in Turbulent Flames”. In : *Journal of Engineering for Gas Turbines and Power* 118.2 (1996), pp. 292–307. DOI: 10.1115/1.2816591.

[36] U. Guven and G. Ribert. “Large-Eddy Simulation of Supersonic Hydrogen/Oxygen Combustion: Application to a Rocketlike Igniter”. In : *Journal of Propulsion and Power* 34.2 (2018), pp. 291–307. DOI: 10.2514/1.B36542.

[37] H. Yamashita, M. Shimada, and T. Takeno. “A numerical study on flame stability at the transition point of jet diffusion flames”. In : *Symposium (International) on Combustion* 26.1 (1996), pp. 27–34. DOI: 10.1016/s0082-0784(96)80196-2.

[38] V. Golovitchev, M. Bergman, and L. Montorsi. “CFD modeling of diesel oil and DME performance in a two-stroke free piston engine”. In : *Combustion Science and Technology* 179.1-2 (2007), pp. 417–436. DOI: 10.1080/00102200600837242.

[39] R. Miake-Lye and J. Hammer. “Lifted turbulent jet flames: A stability criterion based on the jet large-scale structure”. In : *Symposium (International) on Combustion* 22.1 (1989), pp. 817–824. DOI: 10.1016/s0082-0784(89)80091-8.